Superlattices and Microstructures 100 (2016) 1213–1220

Contents lists available at ScienceDirect

Superlattices and Microstructures

journal homepage: www.elsevier.com/locate/superlattices

MnO_2 ultrathin films deposited by means of magnetron sputtering: Relationships between process conditions, structural properties and performance in transparent supercapacitors

Michał A. Borysiewicz*, Marek Wzorek, Marcin Myśliwiec, Jakub Kaczmarski, Marek Ekielski

Instytut Technologii Elektronowej, Al. Lotników 32/46, 02-668 Warszawa, Poland

ARTICLE INFO

Article history:
Received 1 November 2016
Accepted 2 November 2016
Available online 4 November 2016

Keywords:
MnO_2
Magnetron sputtering
Transparent electronics
Supercapacitor
Ultracapacitor
Sputtering
ZnO
Wearable electronics

ABSTRACT

This study focuses on the relationships between the process parameters during magnetron sputter deposition of MnO_2 and the resulting film properties. Three MnO_2 phases were identified - γ, β and λ and the dependence of MnO_2 phase presence on the oxygen content in the sputtering atmosphere was found. Selected MnO_2 phases were subsequently applied as ultrathin coatings on top of nanostructured ZnO electrodes for transparent supercapacitors with LiCl-based gel electrolyte. The films containing λ-MnO_2 exhibited both the highest optical transparency of 62% at 550 nm as well as the highest specific capacitance in the supercapacitor structure, equal to 73.1 μF/cm^2. Initially lower, the capacitance was elevated by charge-discharge conditioning.

1. Introduction

Manganese dioxide is one of the most relevant compounds for modern energy storage devices, applied as electrodes both in the widespread Li-ion batteries [1,2] as well as in supercapacitor structures [3], due to its significant charge storage capabilities combined with chemical stability, abundance and low cost. The material crystallizes in many polymorphic forms, among which α, β, γ, δ and λ are the most known. The forms differ by the crystalline structure, in particular possess different types of angstrom-size tunnels, beneficial for ion intercalation in electrochemical energy storage devices [4]. Most MnO_2 materials are synthesized using the wet-chemical route and the current focus of study lies in MnO_2 nanostructures fabricated by a wide array of methods.

At the same time, there is growing interest in micro power sources, fabricated using conventional microelectronic processing techniques for wearable devices [5]. One of such techniques is magnetron sputtering, compatible with conventional lithography and microprocessing requirements.

* Corresponding author.
E-mail address: mbory@ite.waw.pl (M.A. Borysiewicz).

http://dx.doi.org/10.1016/j.spmi.2016.11.002

There are not much literature information on magnetron sputtering of MnO_2. In 1972 Landorf et al. used an 8″ diameter Mn cathode for deposition of MnO_2 on glass slides in an oxygen atmosphere at 2.7 Pa, using RF voltages of 1.5–3 kV and currents 0–45 mA for application in thin film capacitors [6]. The substrates were kept at temperatures between 140 and 230 °C. X-ray diffraction patterns of the films contained lines that could be ascribed to either β-MnO_2 or γ-MnO_2. The films had densities of around 3.0 g/cm^3, significantly lower than the theoretical 5.0 g/cm^3. Subsequently, in 1994 Fau et al. [7] deposited the material at 200 W RF power using a 80 mm diameter MnO_2 target under 2 Pa total pressure and 13:2 Ar to O_2 flow ratio obtaining, as the previous authors, either β-MnO_2 or γ-MnO_2 phase. In newer reports, Zhang et al. studied MnO_2 on Al_2O_3 for gas sensing purposes [8]. They deposited the material using a 35 mm MnO_2 target under 200 W RF power, 5 Pa total pressure and 9:1 Ar to O_2 flow ratios. Yielding a 'coarse' microstructure on top of the Al_2O_3 substrates used. XRD patterns yielded MnO_2 identified only as 'tetragonal', which most probably is β-MnO_2. Finally, Li et al. studied MnO_2 deposition on copper using a Mn target with reactive deposition in an argon-oxygen mixture (7:3 Ar to O_2 flow ratio and a pressure of 0.8 Pa) and found X-ray amorphous material with small grains of 10 nm diameter, however they did not study the grain structure [9].

These reports focused on single, arbitrary chosen process conditions to deposit the MnO_2 films, and then put more weight on other behavior of the material, e.g. in devices. Therefore, we decided to provide in this communication a systematic study of the process conditions influencing the properties of the MnO_2 films deposited by reactive RF magnetron sputtering, with emphasis on structural properties and phase identification. We decided to combine the properties of the deposited material with the performance of transparent supercapacitors based on nanoporous ZnO electrodes coated with the MnO_2 to meet the common applications of the material.

Transparent power sources are an interesting concept, deriving directly from the rapid development of transparent electronics, in particular transparent displays. In transparent wearable devices (e.g. enhanced contact lenses or glasses) not only the display should be transparent, but also the whole device including the power source. The works concerning transparent supercapacitors focus mostly on very thin carbon film electrodes due to the high capacitance of conventional carbon electrodes. The usual reports see specific capacitances of around 1 mF/cm^2 with transparency around 50% [10,11].

In our investigation, we decided to form the porous electrode using the intrinsically transparent ZnO semiconductor [12] in order to achieve high capacitance through an increased surface area and then to coat it with MnO_2 for capacitance enhancement by ion intercalation. We wanted to see which process parameters would lead to the formation of MnO_2 phases yielding the highest capacitance in such a system. The high transparency of the device is maintained by a low MnO_2 film thickness set at 10 nm.

2. Experimental

The experiment was divided into two parts. First, MnO_2 thin films were deposited by magnetron sputtering and their structural properties were studied. Secondly, a part of the MnO_2 films was selected to be deposited on top of transparent porous ZnO films to be used as transparent electrodes of a supercapacitor.

The MnO_2 sputter deposition was carried out in a Surrey NanoSystems γ-1000C reactor using a 75 mm diameter MnO_2 target under 125 W RF power. The target to substrate distance was 15 cm. In the experiment, the total gas pressure was 0.2, 0.4, 0.8 or 1.6 Pa and the atmosphere was composed of 10 sccm Ar and 0, 1 or 5 sccm of O_2. The total pressure and gas flows were controlled independently by the application of a throttle valve. During sputtering, a Hiden ESPion Langmuir probe was used to monitor the plasma parameters. Film thicknesses and densities were determined using X-ray reflectometry (XRR) on a PANalytical Empyrean 2 equipped with Cu K^{α} radiation, a 2-Ge monochromator with a mirror and a Pixcel detector. Structural information was derived from transmission electron microscopy (TEM) on a JEOL JEM-2100 using imaging and selected area electron diffraction (SEAD) of the material deposited directly on TEM carbon grids. Since the deposition rates were very low, conventional X-ray diffraction was not feasible with the ultrathin films achieved.

Based on the structural analysis, a set of parameters was chosen to deposit 10 nm - thick MnO_2 films on porous ZnO/FTO-glass electrodes and supercapacitors were fabricated. The porous ZnO films of 450 nm thickness were fabricated using magnetron reactive sputtering of a Zn target in an Ar:O_2 atmosphere in the same reactor with postdeposition oxidation in an oxygen flow at 400 °C for 5 min - a process we described earlier [13]. Since the ZnO formed in this manner is highly resistive, a second annealing in an argon-hydrogen mixture was applied to dope the ZnO, as hydrogen forms a shallow donor in ZnO [12]. An optimized temperature of 350 °C and time of 30 s was chosen. The supercapacitors were assembled of two symmetrical electrodes, in-between which a frame of a double-sided 100 μm thick adhesive tape was applied serving both as the electric separator and sealant. A poly(vinyl alcohol) (PVA) and LiCl gel electrolyte was used in the supercapacitors. To prepare the electrolyte, 20 ml of H_2O were heated to 95 °C. Next, 2 g of PVA were added with mechanical mixing. After the mixture became homogeneous, 4.25 g of LiCl were added followed by vigorous mixing. Cyclic voltammetry tests were performed to assess supercapacitor performance using a Gamry Reference 3000 potentiostat. The optical transmission was determined using a Sentech SE 800E spectral ellipsometer. Stability tests were performed for 5000 charge/discharge cycles.

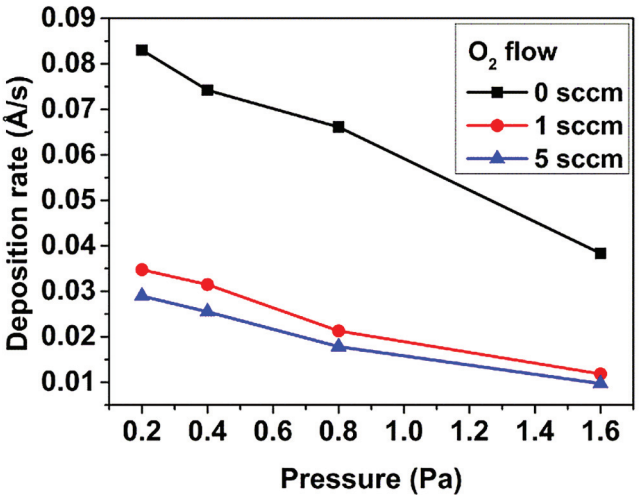

Fig. 1. MnO_2 deposition rate as a function of total gas pressure for three oxygen flows: 0, 1 and 5 sccm, derived using XRR.

3. Results and discussion

3.1. Film characterization

The first important consideration with MnO_2 deposition by RF-sputtering is the very low deposition rate (see Fig. 1) compared with e.g. ZnO, averaging 0.28 Å/s in the same reactor and magnetron configuration under high oxygen content (10 sccm Ar, 5 sccm O_2, 0.8 Pa) and the same RF power of 125 W. However low, the deposition rate drops with both the increase in oxygen flow and total gas pressure as is normally expected during reactive magnetron sputtering.

As shown in Fig. 2, the plasma electron temperature and density determined from Langmuir probe measurements exhibited changes within ranges typical for oxide sputtering on this magnetron (T_e = 2.0–3.0 eV and $N_e = 10^{17}$–$1.6 \cdot 10^{17}$ cm^{-3}). T_e values are the highest for 0.2 Pa and drop with increasing pressure, although at 0.4–1.6 Pa, the values change only very little. Also, apart from the data at 0.2 Pa, there is little difference between T_e for different oxygen flows at the respective pressures. Similarly, the N_e is the lowest at 0.2 Pa and then it rises, but flattens out for the higher pressures. Here, the differences between the data points for each pressure are larger, but still the whole behavior can be described as almost stable. No correlation can be seen between the plasma parameters and deposition rate.

By analyzing the radial intensities of electron diffraction patterns (see Fig. 3a and b) we were able to distinguish three pairs of lines, always appearing together in the patterns. They are related to the following d-spacings: 2.45 Å and 1.39 Å, 2.13 Å and 1.62 Å as well as 2.00 Å and 1.54 Å. We cross-checked the PDF-2 database for possible matches, in particular against MnO (01-071-4748), Mn_3O_4 (00-024-0734) and Mn_2O_3 (03-065-7467) but found no positive correlations for both lines in each pair. We were however able to ascribe the peaks positively to different MnO_2 phases, based on experimental data for nanoparticles by Devaraj et al. [4]. We found therefore, that based on experimental conditions, we were able to fabricate a mixture of three MnO_2 phases: γ (2.45 Å and 1.39 Å), β (2.13 Å and 1.62 Å) and λ (2.00 Å and 1.54 Å). The respective planes are noted in Fig. 3b. A matrix of the observed MnO_2 phases as a function of both oxygen flow and total pressure was created and is presented in Fig. 3c. It is visible, that γ-MnO_2 is always present, independently on the process parameters. The samples deposited at 1.6 Pa and both 1 and 5 sccm O_2 exhibit only γ-MnO_2 lines. However, the strongest intensity of the γ-MnO_2 lines was observed for the film deposited at 0.8 Pa and 1 sccm O_2. With decreasing pressure and oxygen flow – which can be interpreted as generally decreasing oxygen content in the sputtering chamber – β-MnO_2 starts to appear in the samples with its strongest peaks visible for 1 sccm O_2 and total pressures from 0.2 to 0.8 Pa. Then for 0 sccm oxygen the λ phase is present for all total gas pressures and the peaks related to this phase appear to be relatively constant as a function of the pressure.

TEM images taken for the samples show two main crystallite types. Small, agglomerated almost circular ones with an approximated radius of several nm (see Fig. 4a) and long needle-like (see Fig. 4b and c). Looking at high magnification images it can be seen, that the 'needles' are actually more like bent petals with a significant portion laying on the surface and one edge sticking out of the sample plane, creating the needle-type image (see Fig. 4d). By selected area FFT – inverse FFT selection and analysis, we were able to obtain clear images of the crystalline planes and determined the interplanar spacings of the visible crystallites. Both types were found to be γ-MnO_2, the dominant phase in the samples. Furthermore, the median round crystallite size was found to fall with the increasing oxygen flow, with 31–80 nm^2 for 0 sccm, 31–49 nm^2 for 1 sccm and 4–19 nm^2 for 5 sccm. The needle/petal crystallite density is also not uniform with regard to process conditions. Their presence is higher for the 5 sccm O_2 samples than 1 sccm O_2 ones, with their highest density for the 0.8 Pa pressure in both cases. The density drops with the increasing oxygen content as defined previously for β – MnO_2 with no such crystallites visible either in

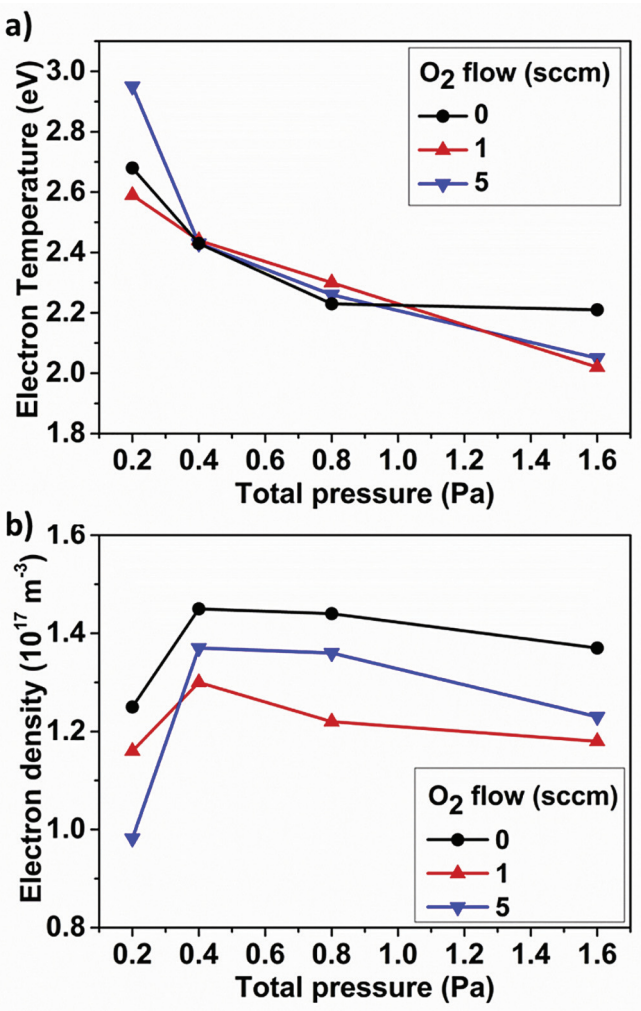

Fig. 2. Electron temperature (a) and electron density (b) derived from Langmuir probe I-V measurements of the plasma discharge during MnO_2 target sputtering, as a function of total gas pressure for three oxygen flows: 0, 1 and 5 sccm.

the sample 1 sccm O_2/0.2 Pa nor in any of the samples for 0 sccm O_2. We were not able to physically identify the crystals of other phases, but this might be due to the overlap of the different crystallites in the specimens used. One may hypothesize, that due to the low thickness of the samples the other crystallites should be very small and would require a higher resolution microscope for a full analysis. However, the captured SAED patterns prove their presence in the samples.

The density of the films was determined using XRR and the results are shown in Fig. 5. The higher the oxygen flow during the experiment, the lower the material density. Taking into consideration the samples grown at 0.8 Pa, for 0 sccm O_2 the density is 5.6 g cm^{-3}, for 1 sccm O_2 it is 4.8 g cm^{-3} and finally for 5 sccm – 4.6 g cm^{-3}. The trends show a slight drop with decreasing pressure and a rise with increasing pressure. These results are far from the 5.0 g cm^{-3} bulk MnO_2 density and relate more to the densities of MnO (5.43 g cm^{-3}), Mn_3O_4 (4.86 g cm^{-3}) and Mn_2O_3 (4.5 g cm^{-3}). Here the samples are however in the form of thin films or rather collections of nanoparticle grains, which also are not completely continuous as seen from TEM images. Although the density of different MnO_2 phases are not well referenced in the literature, an example concerning α-MnO_2 density of 4.21 g cm^{-3} can be found [14] or λ-MnO_2 density of 4.48–4.61 g cm^{-3} [15] showing significant difference from the theoretical 5.0 g cm^{-3}. Taking this into account, the measured densities of the samples can serve as reference.

3.2. Supercapacitor performance

Based on the material characterization data gathered, we chose 5 process parameter sets for the fabrication of 10 nm thick MnO_2 films on sputter deposited nanocrystalline ZnO [13] for application as transparent electrodes in supercapacitors. We chose three samples deposited at 0.8 Pa and 0, 1 and 5 sccm O_2 and the samples grown at 1 sccm O_2 and 0.2 Pa and 1.6 Pa to

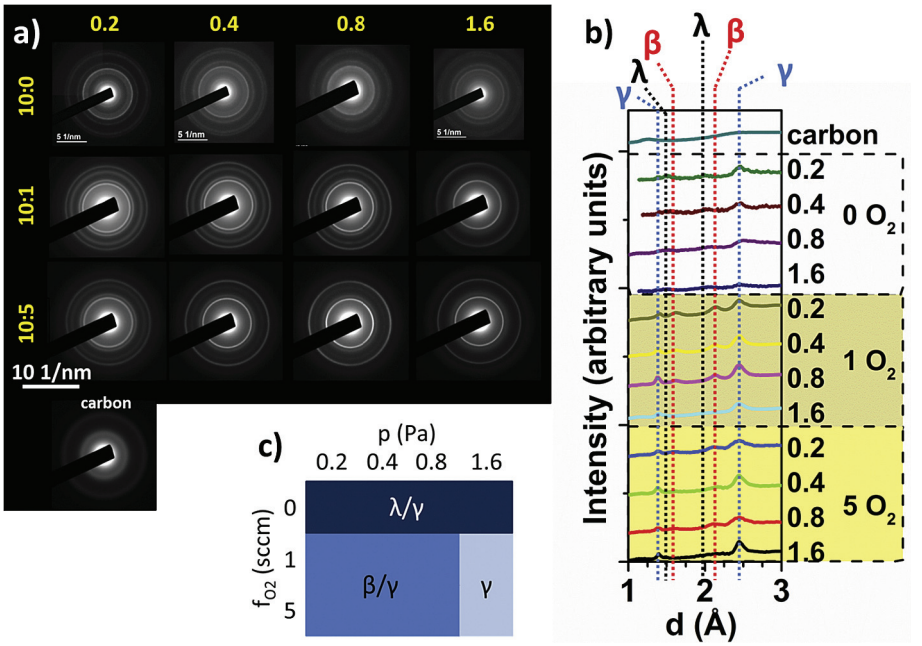

Fig. 3. a) SAED images for the MnO_2 films fabricated in the experiment, deposited directly on TEM carbon grids, as a function of total pressure (columns) and argon to oxygen flow ratios (rows) with the SAED image for the carbon grid itself; b) Intensities of SAED circles as a function of interplanar spacing for the samples, the data is presented for the groups of 0 sccm O_2, 1 sccm O_2 and 5 sccm O_2, each presenting the data for 0.2, 0.4, 0.8 and 1.6 Pa; c) a schematic depiction of the obtained MnO_2 phases in the pressure-oxygen flow parameter space.

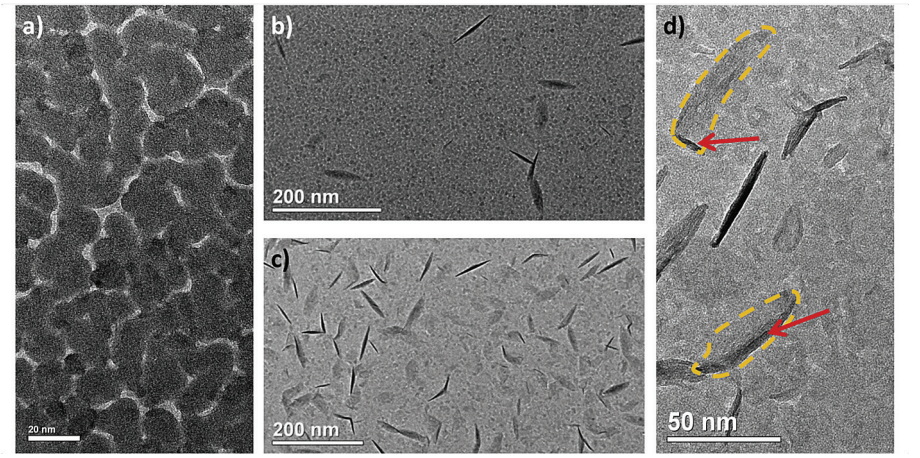

Fig. 4. TEM images of selected samples presenting the nanocrystalline morphologies in the films: a) circular, agglomerated γ-MnO_2 grains (0 sccm O_2, 0.8 Pa); b) circular γ-MnO_2 covered by low density needle/petal γ-MnO_2 (1 sccm O_2, 0.4 Pa); c) circular γ-MnO_2 covered by high density needle/petal γ-MnO_2 (5 sccm O_2, 0.4 Pa); d) large magnification image showing the petal γ-MnO_2 in yellow dashed line, and the needles being petal parts folded out of the sample plane – red arrow (5 sccm O_2, 0.8 Pa). (For interpretation of the references to colour in this figure legend, the reader is referred to the web version of this article.)

cover all MnO_2 phase combinations, constant pressure and oxygen flow considerations and to check for the influence of the needle/petal crystallites on the electrode behavior. For reference, we also added a ZnO electrode, without the MnO_2. The devices were labelled M0 – M5 according to Table 1.

The transmission of the devices, presented in Fig. 6a shows that the maximum transmittances are toward the red end of the visible spectrum and reach 70% for M2. The values at 550 nm which is around the middle of the visible spectrum are presented in Table 1. The device M1 (see Fig. 6b) shows almost identical transmission at this point as M0 based on ZnO. The character of the M1 curve is also specific, similar only to M0 and M4, whereas the other devices have much sharper drops in transmittance when moving to shorter wavelengths.

The results of electrochemical cyclic voltammetry are presented in Fig. 6c. The cyclic voltammograms of the devices show an almost rectangular shape for the ZnO supercapacitor, indicating a close to ideal capacitor behavior, with only a minor slope,

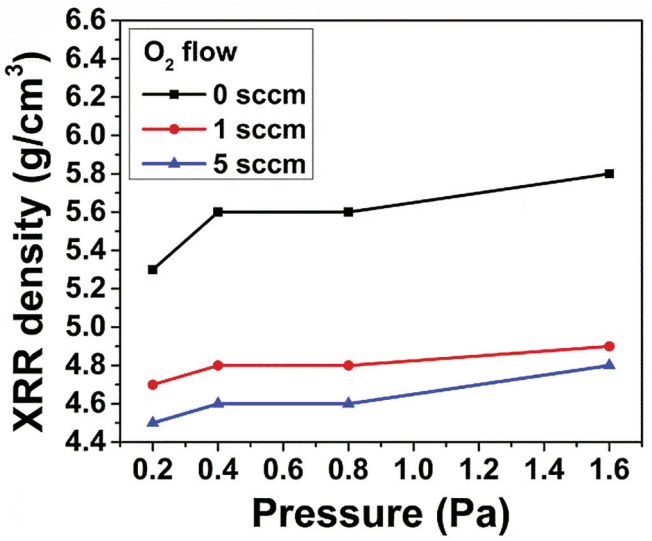

Fig. 5. MnO_2 film density derived from XRR as a function of total gas pressure for three oxygen flows: 0, 1 and 5 sccm.

indicating that the device is not behaving like a resistor. All devices containing MnO_2 had lower capacitances than M0, which is probably due to ZnO pore encapsulation through the deposition of the 10 nm MnO_2 film, lowering the available surface for ion penetration. It can be noted that the only device presenting currents close to those of pure ZnO-based device is M1. It is also the one with the strongest nonlinearity. The nonlinearity, visible also in the bottom part of all MnO_2 devices indicates some degree of redox reactivity, as would be expected from MnO_2. The reactions are reversible since the cyclic voltammetry curves exhibited no changes in the subsequent cycles (not shown).

By integrating the I-V characteristics and dividing them by the sweep rate, the effective capacitances of the devices were determined, (see Fig. 6d). At this point it is worthwhile to try to correlate the structural properties of the MnO_2 films with device performance. Considering first the samples deposited at the same pressure of 0.8 Pa and different oxygen flows from 0 to 5 sccm (M1, M3, M5) one can see that with increasing flow the capacitance of the device drops. This can be related to the phases visible in the films with λ-MnO_2/γ-MnO_2 in M1, β-MnO_2/γ-MnO_2 in M3 and M5. Taking into account that the density of needle/petal γ-MnO_2 crystallites is the highest in samples deposited at 0.8 Pa and 5 sccm O_2, we could relate the lowest C_{eff} of the M5 device to their presence. The same relationship follows not only for C_{eff} but also for transmittance. However, considering the samples deposited at 1 sccm O_2 flow and different pressures, their capacitance is maximum for the sample deposited at 0.8 Pa, having the highest needle/petal density of the samples deposited at 1 sccm O_2. On the other hand, the capacitance can be correlated with the intensity γ-line in the SAED patterns in Fig. 3 as for M2-M4 as for M5. It can be said that the more well pronounced the line, the capacitance is higher, except for the M1 case where the presence of λ-MnO_2 takes over. One can also notice the apparent correlation between the material density and capacitance. The higher the density, the higher the C_{eff} (except M4) which can be attributed to higher densities of materials with smaller pores, which in turn are more efficient at charge storage.

The sample M1, containing λ-MnO_2 presents by far the best MnO_2 device performance. The reason for this might be that λ-MnO_2 is isostructural with $LiMn_2O_4$ with extracted Li^+ ions [16], a material with high capability of Li^+ intercalation, which is used as an electrode in Li-ion batteries. Furthermore, the capacitance of the M1 supercapacitor with the λ-MnO_2 phase rose significantly after 100 galvanostatic charge-discharge cycles with 10 μA constant current (see Fig. 6e), placing itself above that of pure ZnO electrodes. After that rise, the C_{eff} remained constant for the next 4900 cycles – capacitance retention of 95% was registered. This effect was not recorded for other samples, although they all exhibited highly stable capacitance values with a capacitance retention of 85–92%. The cyclic voltammograms of the M1 in the range 0–1 V before and after the change are presented in Fig. 6f. Not only are the mean current values greater but also the character of the curve is changed. In the initial characteristic two broad peaks at 0.70 V and 0.34 V can be seen, which may represent Li^+ intercalation and removal. The values are similar to those reported in the literature for ZnO/MnO_2 electrodes, although in Na_2SO_4 aqueous electrolyte for an undetermined MnO_2 phase [17]. After the change, the peaks disappear and only one broad peak is visible, centered around 0.43 V in the returning bias sweep. The character of the curve during the bias sweep up is reminiscent of a situation where a peak is present at a voltage above 1 V. We expect that the observed chemical reaction is related to the intercalation of Li^+ in λ-MnO_2 and a formation of $LiMn_2O_4$-related material. Indeed for $LiMn_2O_4$ in LiCl electrolyte the peaks for intercalation and removal of Li^+ reported in the literature are around 1.1 V and 0.5 V, respectively [18] which is reasonably close to the values in this experiment. With the change in electrochemical behavior, the transparency of the device grows in all wavelength range. E.g. it rises by 20% - from 0.52 to 0.62 at 550 nm. The band gap derived from the transparency measurements of the supercapacitor does not change significantly - from

Table 1
List of the MnO_2 samples selected for supercapacitor tests.

Sample type	MnO_2 phases	O_2 flow (sccm)	Deposition pressure (Pa)	MnO_2 density (g/cm^3)	C_{eff} (μF/cm^2)	T @ 550 nm
M0	ZnO without MnO_2				45.6	0.53
M1	λ/γ	0	0.8	5.6	35.0/73.1[a]	0.52/0.63[a]
M2	β/γ	1	0.2	4.7	18.1	0.43
M3	β/γ	1	0.8	4.8	25.1	0.38
M4	γ	1	1.6	4.9	11.0	0.50
M5	β/γ	5	0.8	4.6	13.2	0.32

[a] The device M1 increased its capacitance and transparency after 100 charge/discharge cycles.

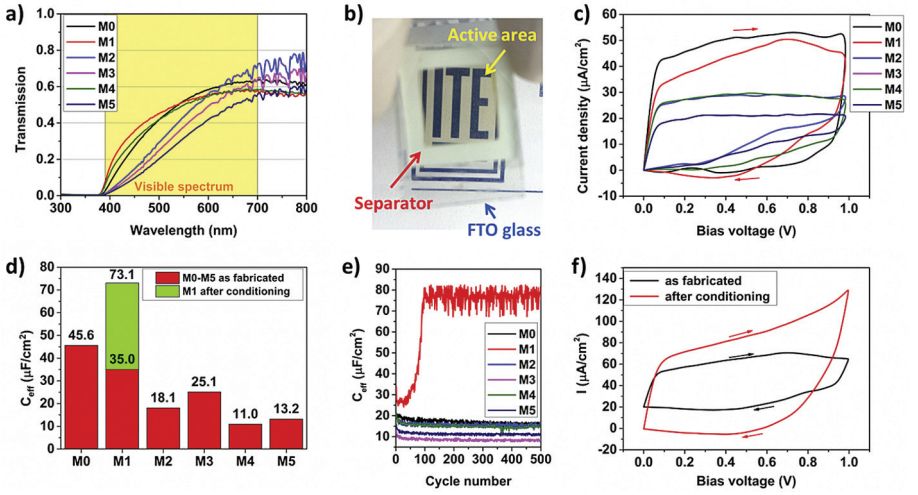

Fig. 6. Characterization results of the supercapacitor devices M0 – M5. a) Optical transmission for the devices; b) Image of the M1 device; c) cyclic voltammetry plots of the devices with 1V/s sweep rate; d) effective capacitance derived from the integration of the cyclic voltammetry plots; e) capacitance for low, 10 μA, charge/discharge current as a function of charge-discharge cycles; f) cyclic voltammetry plots of the M1 device as fabricated and after the initial conditioning of 100 charge-discharge cycles.

3.21 eV for the device with λ-MnO_2 to 3.24 eV for the device with the new material and it is the band gap of ZnO. The band gap values reported in the literature for $LiMn_2O_4$ vary significantly from 1.77 to 2.42 eV [19] for Density Functional Theory calculations for bulk and from 1.43 eV [20] to 1.63 or 2.00 eV [21] determined experimentally for nanocrystalline $LiMn_2O_4$. It is significantly greater than the 0.3 eV reported for MnO_2 [22]. The increase in transparency can be therefore related to an increase in the band gap.

4. Conclusions

The properties of thin MnO_2 films deposited using magnetron sputtering of a MnO_2 target were studied in a wide range of process conditions. It was found, that the material crystallizes in three types of phase composition, depending on the oxygen content in the chamber during sputtering (relating to both the oxygen flow and total gas pressure). For no oxygen content a composition of λ-MnO_2/γ-MnO_2 was found. For intermediate oxygen content the composition changed to β-MnO_2/γ-MnO_2 and for the largest oxygen content the γ-MnO_2 phase was dominating. It was found that the γ-MnO_2 had two morphologies – a circular one, comprising most of the film, and a flat 'petal'-like one, scattered on the surface of the film. Some of the petals had one of their edges at a normal angle to the substrate and their concentration diminished with decreasing oxygen content. 10 nm thick MnO_2 films were introduced in transparent supercapacitor electrodes based on nanostructured ZnO. Instead of enhancing the capacitor performance, all of them yielded lower capacitances than those observed for uncoated ZnO electrodes. This might be due to MnO_2 covering the pores of the ZnO thus reducing the electrode area. However, the λ-MnO_2/γ-MnO_2 phase yielded the highest capacitancies of all samples with MnO_2 coating, close to that of ZnO. Subsequently, after 100 charge-discharge cycles, the capacitance of this device rose significantly to 160% of the capacitance of the ZnO device and remained stable for the next 4900 charge-discharge cycles. We believe this behavior was due to an electrochemical reaction transforming the λ-MnO_2/ZnO system into a $LiMn_2O$-based nanostructure. However, further studies are required to exactly explain the change which took place.

Acknowledgments

This work was carried out in the frames of the NACZO project [23], supported by the Polish National Centre for Research and Development (NCBiR) under Grant No. LIDER/030/615/L-5/NCBR/2014.

References

[1] X. Guo, J. Han, L. Zhang, P. Liu, A. Hirata, L. Chen, T. Fujita, M. Chen, Nanoscale 7 (2015) 15111–15116, http://dx.doi.org/10.1039/C5NR05011A.
[2] S. Deng, L. Wang, T. Hou, Y. Li, J. Phys. Chem. C 119 (2015) 28783–28788, http://dx.doi.org/10.1021/acs.jpcc.5b10354.
[3] M. Huang, F. Li, F. Dong, Y.X. Zhang, L.L. Zhang, J. Mater. Chem. A 3 (2015) 21380–21423, http://dx.doi.org/10.1039/C5TA05523G.
[4] S. Devaraj, N. Munichandraiah, J. Phys. Chem. C 112 (2008) 4407–4417, http://dx.doi.org/10.1021/jp7108785.
[5] S. Ferrari, M. Loveridge, S.D. Beattie, M. Jahn, R.J. Dashwood, R. Bhagat, J. Power Sources 286 (2015) 25–46, http://dx.doi.org/10.1016/j.jpowsour.2015.03.133.
[6] R.W. Landorf, S.J. Licht, J. Electrochem. Soc. 119 (1972) 430–433, http://dx.doi.org/10.1149/1.2404223.
[7] P. Fau, J.P. Bonino, A. Rousset, Appl. Surf. Sci. 78 (1994) 203–210, http://dx.doi.org/10.1016/0169-4332(94)00111-1.
[8] C. Zhang, A. Boudiba, C. Navio, M.-G. Olivier, R. Snyders, M. Debliquy, Sensors Actuators B 161 (2012) 914–922, http://dx.doi.org/10.1016/j.snb.2011.11.062.
[9] Y. Li, H. Xie, J. Li, J. Wang, Mater. Lett. 102–103 (2013) 30–32, http://dx.doi.org/10.1016/j.matlet.2013.03.098.
[10] K. Gao, Z. Shao, X. Wu, X. Wang, Y. Zhang, W. Wang, F. Wang, Nanoscale 5 (2013) 5307–5311, http://dx.doi.org/10.1039/C3NR00674C.
[11] J. Ge, G. Cheng, L. Chen, Nanoscale 3 (2011) 3084–3088, http://dx.doi.org/10.1039/C1NR10424A.
[12] A. Janotti, C.G. van de Walle, Rep. Prog. Phys. 72 (2009) 126501, http://dx.doi.org/10.1088/0034-4885/72/12/126501.
[13] M.A. Borysiewicz, E. Dynowska, V. Kolkovsky, J. Dyczewski, M. Wielgus, E. Kamińska, A. Piotrowska, Phys. Stat. Sol. A 209 (2012) 2463–2469, http://dx.doi.org/10.1002/pssa.201228041.
[14] Dale L. Perry, Handbook of Inorganic Compounds, second ed., CRC Press, 2011. ISBN 9781439814611.
[15] W.L. Bowden, K. Brandt, P.A. Christian, Z. Jiang, United States Patent 6,759,167, July 6, 2004.
[16] Helena Berg, Håkan Rundlöv, John O. Thomas, Solid State Ionics 144 (2001) 65–69, http://dx.doi.org/10.1016/S0167-2738(01)00894-3.
[17] P. Yang, X. Xiao, Y. Li, Y. Ding, P. Qiang, X. Tan, W. Mai, Z. Lin, W. Wu, T. Li, H. Jin, P. Liu, J. Zhou, C. Ping Wong, Z.L. Wang, ACS Nano 7 (2013) 2617–2626, http://dx.doi.org/10.1021/nn306044d.
[18] M. Jayalakshmi, M. Mohan Rao, F. Scholz, Langmuir 19 (2003) 8403–8408.
[19] K. Hoang, arXiv: 1412.5264v1 [cond-mat.mtrl-sci] 17 Dec 2014.
[20] M. Raja, S. Mahanty, P. Ghosh, R. Basu, H. Maiti, Mater. Res. Bull. 42 (2007) 1499–1506.
[21] K. Kushida, K. Kuriyama, Appl. Phys. Lett. 77 (2000) 4154–4156.
[22] A.K.M. Farid ul Islam, R. Islam, K.A. Khan, J. Mater. Sci. Mater. Electron 16 (2005) 203–207.
[23] http://www.naczo.ite.waw.pl.